

Low-temperature properties of CeAu₂Ge₂ single crystals grown from Au-Ge and Sn flux

C. L. Huang,^{1,2,*} V. Fritsch,² W. Kittler,² and H. v. Löhneysen^{1,2}

¹Karlsruher Institut für Technologie, Institut für Festkörperphysik, 76021 Karlsruhe, Germany

²Karlsruher Institut für Technologie, Physikalisches Institut, 76031 Karlsruhe, Germany

(Received 29 May 2012; revised manuscript received 2 August 2012; published 3 December 2012)

The specific heat of CeAu₂Ge₂ single crystals grown from Au-Ge (AGF) or Sn flux (SF) was measured at temperatures T between 1.8 and 200 K. Two magnetic transitions are observed in the zero-field specific heat at 12.1 and 14.5 K in the AGF sample, while only a single sharp transition at 9.2 K is seen in the SF sample, confirming our recent susceptibility results [Fritsch *et al.*, *Phys. Rev. B* **84**, 104446 (2011)]. We observe several field-induced transitions in the magnetoresistance of the AGF sample measured at 1.6 and 2.3 K in accordance with the B - T phase diagram constructed from isothermal magnetization curves $M(B)$. In addition, we have measured $M(B)$ under hydrostatic pressure P up to 10.5 kbar. The Néel temperature T_N increases linearly with P at a small rate of 0.049 K/kbar, which suggests that, if $T_N(P)$ is attributed to a pure volume effect, this compound is close to the maximum transition temperature of the Doniach diagram. The transition fields B_M between the field-induced phases increase linearly with P as well. The comparable Grüneisen parameters of T_N and B_M indicate that the energy scale depending on the sample's volume is given by the antiferromagnetic correlations and not by the Kondo effect. We discuss possible reasons for the different magnetic behavior of AGF and SF samples.

DOI: [10.1103/PhysRevB.86.214401](https://doi.org/10.1103/PhysRevB.86.214401)

PACS number(s): 75.30.Kz, 74.62.Fj, 75.50.Ee, 75.40.—s

I. INTRODUCTION

Ce-based ternary intermetallic compounds with ThCr₂Si₂ structure reveal a wide variety of magnetic ground states, including antiferromagnetic order, e.g., in CeAu₂Si₂,¹ heavy-fermion quantum criticality, e.g., in CeNi₂Ge₂,² unconventional superconductivity, e.g., in CeCu₂Si₂,³ antiferromagnetism in CeCu₂Ge₂ (Ref. 4) and CePd₂Si₂ (Ref. 5) giving way to superconductivity under pressure, and unconventional metamagnetism, e.g., in CeRu₂Si₂.⁶ In these CeT₂X₂ compounds, where T is the transition metal and $X = \text{Si or Ge}$, the competition between the indirect exchange interactions of Ce $4f$ electrons through the Ruderman-Kittel-Kasuya-Yosida (RKKY) interaction and quenching of the $4f$ magnetic moments due to the Kondo effect or valence fluctuations plays a prominent role in their diverse physical properties.⁷ This variety may be attributed to the decisive effect of the hybridization between $4f$ -electron and conduction-electron states, which for isoelectronic Ce ligands translates to a strong volume dependence of the RKKY and Kondo interactions. Hence, the ground state decisively depends on ionic radius of the T and X atoms.⁸ For example, CeAu₂Si₂ has a large unit-cell volume $V = 189.2 \text{ \AA}^3$, orders antiferromagnetically at $T_N = 8.8 \text{ K}$, and the Kondo effect is reported to be weak ($T_K = 1.7 \text{ K}$),⁹ while CeCu₂Si₂ with a smaller $V = 167.1 \text{ \AA}^3$ is at the brink of antiferromagnetism and superconductivity with $T_c \approx T_N \approx 0.7 \text{ K}$ and $T_K \approx 10 \text{ K}$.¹⁰ The competition between these two different (and here mutually exclusive) ground states in CeCu₂Si₂ is governed by tiny structural changes.¹¹

Polycrystalline CeAu₂Ge₂ was reported to order antiferromagnetically at $T_N \approx 16 \text{ K}$ at ambient pressure.¹² Recent experiments on single crystals revealed that the magnetization is strongly anisotropic with the easy axis being the tetragonal c axis.^{13,14} While these overall features were observed for samples grown from Bi flux (Ref. 13) as well as from Sn and Au-Ge flux,¹⁴ strong differences in the detailed magnetic

properties, including a notable difference of T_N , were found. While Bi- and Sn-flux grown samples (abbreviated as BF and SF, respectively) exhibit only a single metamagnetic transition for $B \parallel c$, several intermediate phases in the magnetization were discovered in Au-Ge flux (AGF) samples.¹⁴ In our previous work,¹⁴ we had done a careful structural and chemical analysis which revealed the following main features. X-ray diffraction showed slightly larger lattice constants of AGF samples ($a = 4.3924 \text{ \AA}$, $c = 10.469 \text{ \AA}$) compared to SF samples ($a = 4.3807 \text{ \AA}$, $c = 10.446 \text{ \AA}$). Both samples showed a slight off-stoichiometric ratio of Au:Ge site occupation (0.962:1.045 for AGF and 0.919:1.01 for SF samples normalized to Ce stoichiometry). The much lower Au site occupation of SF samples was confirmed by EDX measurements revealing a composition of 1.034 (Ce), 1.875 (Au), and 1.893 (Ge) with 4.0 at. % of Sn. The corresponding numbers for the AGF crystals were 1.028, 1.978, and 1.995. This indicates that 4.0 at. % of Sn are incorporated into the SF-CeAu₂Ge₂ crystal. All above values represent the mean of two samples each of the AGF and SF series. In addition, we detected $\lesssim 3$ vol % inclusions of respective flux in both types of samples.

In this study, we present measurements of the electrical resistivity, magnetoresistance, and specific heat of SF and AGF samples which confirm the complex phase diagram of the latter. Our work provides strong additional evidence of the different magnetic behavior of AGF and SF samples, although we can not draw definite conclusions on the origin of these differences. A further aim of this work is to investigate the effect of hydrostatic pressure on the magnetization of the AGF sample in view of the different unit-cell volumes $V_{\text{AGF}} = 202.0 \text{ \AA}^3$ and $V_{\text{SF}} = 200.5 \text{ \AA}^3$ since pressure is a simple yet powerful tool to vary the $4f$ -electron-conduction-electron exchange interaction without introducing additional atomic disorder. We determined the pressure dependence of T_N and of the isothermal magnetization of AGF-CeAu₂Ge₂. Comparisons with other CeT₂X₂ systems are made, and the

evolution of the plateaux in the magnetization of the different phases of the AGF sample with pressure is discussed.

II. EXPERIMENT

The CeAu_2Ge_2 single crystals used in this study were different samples from the same batch as that investigated previously, denoted as AGF VF474 and SF VF467 in Ref. 14. The standard four-probe method was applied to measure the electrical resistivity ρ ($f = 16$ Hz) in the temperature range 1.6–300 K and in magnetic fields up to 6 T. The specific heat C was measured using a Physical Property Measurement System (PPMS, Quantum Design) in the temperature range 1.8–200 K and in magnetic fields up to 6 T. The pressure-dependent magnetization $M(T)$ in $B = 0.1$ T and the magnetization curves $M(B)$ were measured using a CuBe cell in a vibrating-sample magnetometer (VSM, Oxford Instruments) in the temperature range 1.6–300 K and in magnetic fields up to 8 T. The sample of a size of 2–3 mm³ was put into a teflon capsule together with a small piece of Sn used as a manometer, and then the teflon capsule was mounted in a clamp-type CuBe cell using Daphne 7373 oil as a pressure-transmitting medium. The background magnetization of the empty cell was determined in separate runs and was subtracted from the raw data to obtain the sample's contribution. The agreement between two measurements close to 8 kbar can be taken as a demonstration of the reproducibility of the magnetization data under pressure (see Fig. 8). Magnetic fields were applied parallel to the easy axis, i.e., the c axis, in all experiments reported in this paper.

III. RESULTS

A. Electrical resistivity

The electrical resistivity $\rho(T)$ of AGF- and SF- CeAu_2Ge_2 normalized to the value ρ_{300} at $T = 300$ K, as measured with the current applied perpendicular to the c axis, are shown in Fig. 1. At zero field, both samples show that $\rho(T)$ exhibits a broad hump centered around 150 K [see insets of Figs. 1(a) and 1(b)]. For the SF sample, a field of 0.05 T was applied below 5 K to suppress the superconductivity of Sn inclusions, which shows a transition in $\rho(T)$ at 3.6 K. Comparison with the data of LaAu_2Ge_2 from Ref. 13 suggests that the broad hump can be attributed to electron scattering by crystal-electric-field (CEF) excitations, on top of the increase of $\rho(T)$ between 20 and 300 K due to scattering by phonons (see below for the CEF analysis of the specific heat). The residual-resistivity-ratio (RRR) values between $T = 300$ and 1.6 K are 2.6 and 3.0 for the AGF and the SF samples, respectively. The residual resistivity of $18 \mu\Omega \text{ cm}$ at $T = 1.6$ K for the AGF sample is roughly two times smaller than that reported by Joshi *et al.* for BF- CeAu_2Ge_2 .¹³ For the SF sample, the resistivity is four to five times larger than that of the AGF sample, implying pronounced scattering of conduction electrons by about 4% excess of Sn as impurities and about 8% deficiency at the Au site.¹⁴ In AGF- CeAu_2Ge_2 , the resistivity $\rho(T)$ changes its slope at $T_N = 14$ K due to the onset of antiferromagnetic order. We note that a weak maximum of $\rho(T)$ at zero field was observed previously for an AGF sample.¹³ T_N is increasingly suppressed with magnetic field. In SF- CeAu_2Ge_2 , at $T_N = 9.2$ K, $\rho(T)$ shows only a very small change in slope, which

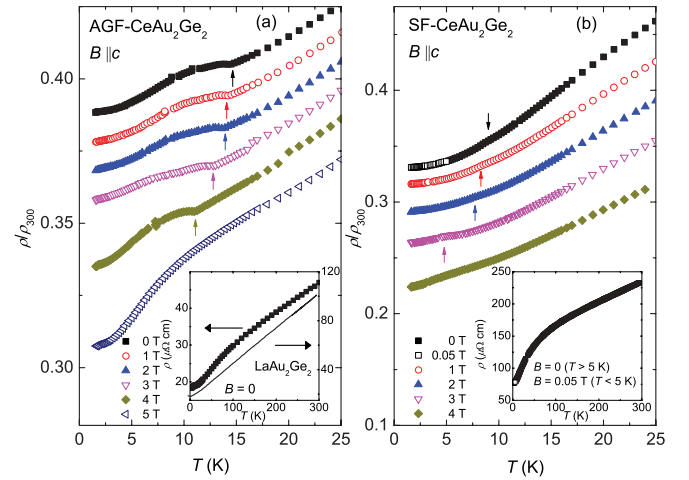


FIG. 1. (Color online) Electrical resistivity $\rho(T)$ of (a) AGF- CeAu_2Ge_2 and (b) SF- CeAu_2Ge_2 normalized to their values ρ_{300} at 300 K in magnetic fields between 1.6 and 25 K. The data ≥ 1 T are shifted consecutively downward by 0.01 in (a) and 0.04 in (b) for clarity. Arrows indicate the T_N 's which are determined at the slope change of $\rho(T)$. Insets show $\rho(T)$ in zero field from 300 to 1.6 K ($B = 0.05$ T is applied when $T < 5$ K in SF- CeAu_2Ge_2 to suppress the superconductivity of Sn).

is indicated by arrows in Fig. 1(b). T_N is totally suppressed at $B = 4$ T.

For AGF and SF samples in the temperature range below 7 and 5 K, respectively, the zero-field resistivity indicates coherent Fermi-liquid behavior $\rho(T) = \rho_0 + AT^2$ due to electron-electron interactions, as can be viewed in a $\rho(T)$ versus T^2 plot in Fig. 2. For the data of $B = 4$ T in the SF sample, the upper limit of validity of the above equation is shrunk to below 4 K. The coefficient A as a function of the magnetic field B is plotted in the insets of Fig. 2, from which we observe a strong enhancement of A when B approaches the critical field B_C (see Fig. 7), which is frequently observed at a

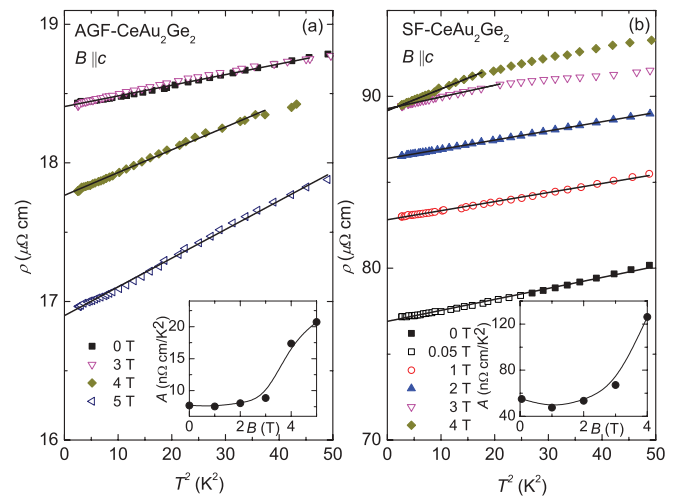


FIG. 2. (Color online) Electrical resistivity $\rho(T)$ vs T^2 of (a) AGF- CeAu_2Ge_2 and (b) SF- CeAu_2Ge_2 . The data of $B = 1$ and 2 T in (a) are omitted for clarity. Solid lines represent the best fit of $\rho(T) = \rho_0 + AT^2$ [the fit of $B = 3$ T in (a) is omitted for clarity], and the coefficient A as a function of magnetic fields is plotted in insets.

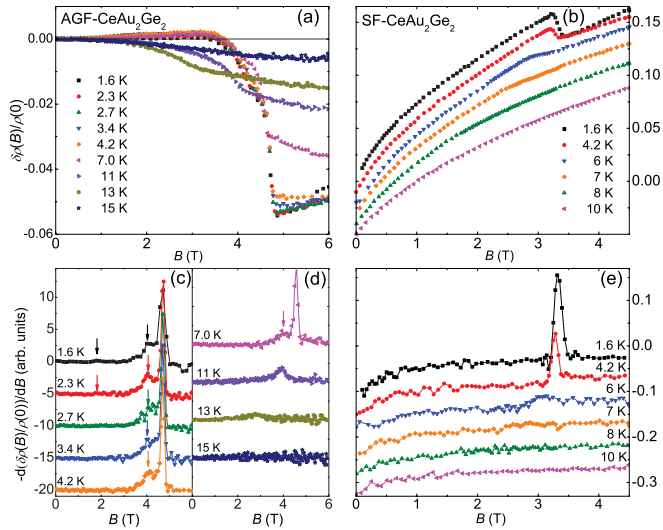


FIG. 3. (Color online) (a) and (b) show magnetoresistance $\delta\rho(B)/\rho(0) = [\rho(B) - \rho(B=0)]/\rho(B=0)$ of AGF- and SF-CeAu₂Ge₂ at different fixed temperatures. The data > 1.6 K are shifted consecutively downward by 0.01 in (b) for clarity. (c), (d), and (e) show differential plots of (a) and (b) as $-d[\delta\rho(B)/\rho(0)]/dB$ vs B . The data for $T > 1.6$ K are shifted consecutively downward by 5 units in (c) and (d) and 0.05 units in (e) for clarity. Arrows indicate the transitions in addition to sharp antiferromagnetic transitions in AGF CeAu₂Ge₂.

field-induced quantum critical point. For $B > B_C$, the $\rho(T)$ of the SF sample can be better described by a linear T dependence below 12 K [see Fig. 1(b)].

The magnetoresistance $\delta\rho(B)/\rho(0)$ where $\delta\rho(B) = \rho(B) - \rho(0)$ is shown in Fig. 3 for different temperatures. We should stress that the $\delta\rho(B)/\rho(0)$ behavior is very different for the SF sample compared to the AGF sample. This is due to the strong positive $\delta\rho(B)/\rho(0)$ from Sn inclusions (see the following). In AGF-CeAu₂Ge₂, for low T and zero or moderate B , $\delta\rho(B)/\rho(0)$ is positive as expected for a coherent Fermi liquid (Kohler's rule). For $T > T_N$, the negative magnetoresistance occurs as a result of the suppression of spin fluctuations upon increasing magnetic fields, which reduces the scattering of electrons. The negative magnetoresistance is also observed in other Ce-based antiferromagnetic heavy-fermion systems, such as CeCu₂Si₂,¹⁵ CeAl₂,¹⁶ CeAl₃,¹⁵ and CeNiGe₃,¹⁷ where the magnetic fields suppress incoherent Kondo scattering. For $T < T_N$, the resistivity shows a decrease which turns into a very sharp transition around 4.8 T at low T and corresponds to the field-induced metamagnetic transition in the magnetization (see Fig. 9 below).¹⁴ For the $T = 1.6$ and 2.3 K data, three field-induced transitions can be determined from intersections of linear fits to the $\delta\rho(B)/\rho(0)$ data around the slope change of Fig. 3(a). They are indicated as arrows in the derivative plot of $-d[\delta\rho(B)/\rho(0)]/dB$ shown in Fig. 3(c). Apart from a subtle transition at $B = 2.3$ T observed in the isothermal magnetization $M(B)$ in Ref. 14, which we fail to see in $\rho(B)$ due to the limited experimental resolution, all other transitions are in accordance with those previously found as can be seen from the B - T phase diagram in Fig. 7(a). In SF-CeAu₂Ge₂, for $T = 1.6$ and 4.2 K, $\delta\rho(B)/\rho(0)$ is positive and about two orders of magnitude larger than the low- T $\delta\rho(B)/\rho(0)$ in the

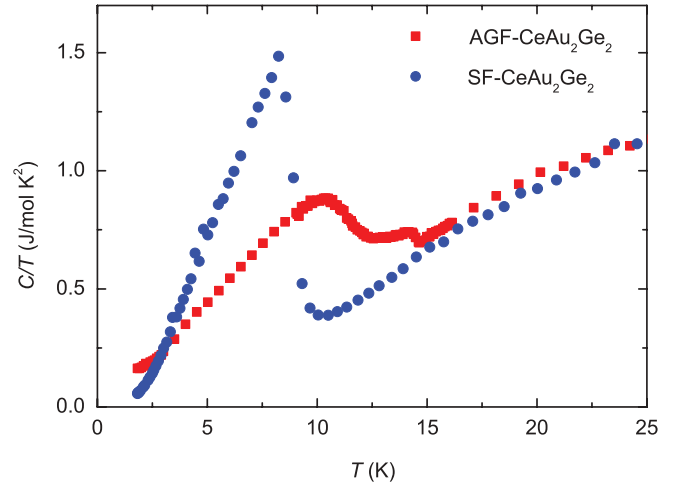


FIG. 4. (Color online) Specific heat C of SF- and AGF-CeAu₂Ge₂ in zero magnetic field plotted as C/T vs T .

AGF sample. There is only one sharp transition observed and the transition is smeared out as $T \geq 6$ K. Above $T_N = 9.2$ K, the whole feature of $\delta\rho(B)/\rho(0)$ is similar to that below T_N . The very large positive $\delta\rho(B)/\rho(0)$ is observed for all temperatures up to 10 K. This is attributed to the pronounced positive magnetoresistance of Sn, which amounts to 100% at $B = 4.5$ T at $T = 4.2$ K.¹⁸

B. Specific heat

The low-temperature specific heat $C(T)$ of AGF and SF-CeAu₂Ge₂ is shown in Fig. 4. A specific-heat jump with the midpoint at $T = 9.2$ K in the SF sample and two anomalies at 12.1 and 14.5 K in the AGF sample confirm the bulk antiferromagnetic ordering nature and underscore the differences between the two types of samples. The transition temperatures are in good agreement with our previous magnetization measurements.¹⁴ The Sommerfeld coefficient γ obtained from the intercept of a linear fit in the C/T versus T^2 plot (not shown) yields roughly 120 mJ/mol K² for the AGF sample which is about one order of magnitude larger than γ of the SF sample. The origin of the large difference is not clear in the present stage. The Kadowaki-Woods ratio A/γ^2 taken from the zero-field data in the magnetically ordered state is $5.3 \times 10^{-7} \mu\Omega \text{ cm} (\text{mol K/mJ})^2$, i.e., 20 times smaller than the value of $\sim 1.0 \times 10^{-5} \mu\Omega \text{ cm} (\text{mol K/mJ})^2$ of heavy-fermion metals.¹⁹ Although A for the SF sample is larger than for the AGF sample (see Fig. 2), γ is at least 10 times smaller, implying that the large A is not due to heavy quasiparticles.

In order to analyze our specific-heat data more closely, we describe the total specific heat between 25 and 200 K by $C_{\text{total}} = C_E + C_{Ph} + C_{\text{CEF}}$, where C_E is the electronic contribution, C_{Ph} is the phonon contribution including Einstein and Debye terms,¹³ and C_{CEF} represents the contribution arising from CEF excitations (see the following). This fit assumes that the full entropy $R \ln 2$ of the Ce crystal-field doublet ground state is reached at 25 K. The obtained parameters, $\gamma = 17$ and 7 mJ/mol K², the Einstein temperature $\Theta_E = 74$ and 78 K, and the Debye temperature $\Theta_D = 312$ and 297 K, for AGF- and SF-CeAu₂Ge₂, respectively, are comparable with

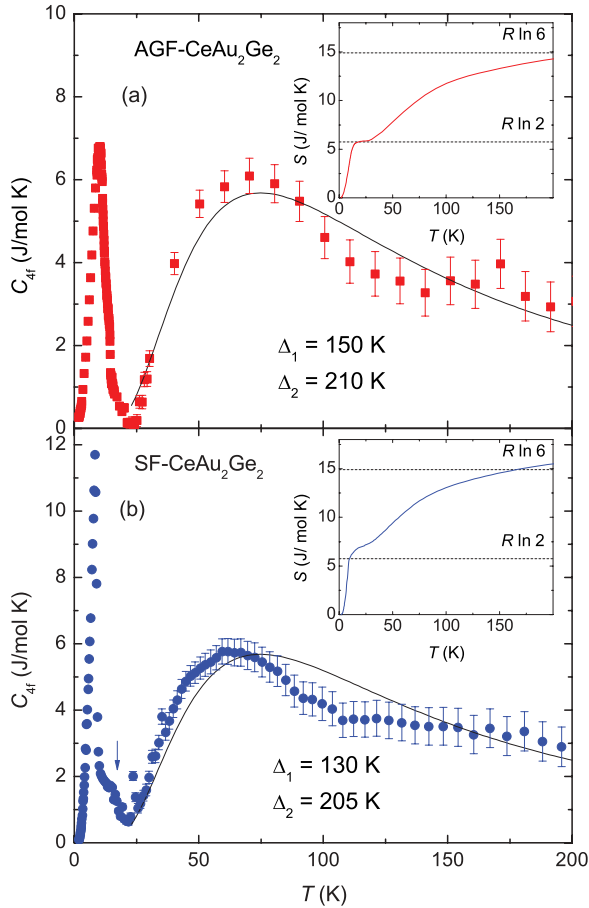


FIG. 5. (Color online) Magnetic contribution to the specific heat C_{4f} vs temperature T of (a) AGF- and (b) SF-CeAu₂Ge₂ together with Schottky fits (see text for details). Error bars indicate $\pm 0.5\%$ of the total specific heat. Insets show the Ce 4*f* entropy S_{4f} vs T in the same temperature region. The arrow in (b) indicates the weak shoulder (see text).

those reported for nonmagnetic LaAu₂Ge₂,¹³ supporting the validity of the present analysis.

By subtracting the electronic and phonon terms from the total specific heat, the Ce 4*f* contribution to the specific heat $C_{4f}(T)$ in the temperature range of 1.8–200 K of AGF- and SF-CeAu₂Ge₂ is obtained as shown in Fig. 5. The resulting maxima around 75 K are due to Schottky-type specific-heat anomalies arising from the splitting of the $J = \frac{5}{2}$ multiplet into three doublets, which are included in the analysis of the total specific heat described above. The best fit yields the energy splittings from the ground state $\Delta_1 = 150$ K and $\Delta_2 = 210$ K for the AGF sample, and $\Delta_1 = 130$ K and $\Delta_2 = 205$ K for the SF sample. These fits are plotted as solid curves in Fig. 5. The obtained energy splittings are in a good agreement with the CEF analysis of the magnetic susceptibility in Refs. 13 and 14. The entropy $S = \int_0^T [C_{4f}(T)/T]dT$ for the two samples is shown in the insets of Fig. 5. In AGF and SF samples, the entropy at $T_{N2} = 14.5$ K and $T_N = 9$ K, respectively, reaches the value of 5.6 J/mol K, which is close to $R \ln 2$ of the doublet ground state, and at 200 K the value of $R \ln 6$ as expected theoretically, thus justifying the assumption used in our fitting procedure.

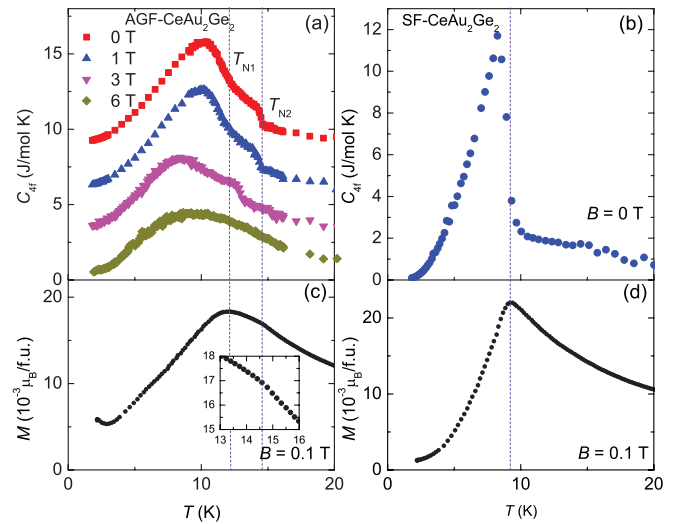


FIG. 6. (Color online) Ce 4*f* contribution C_{4f} to the specific heat of (a) AGF- and (b) SF-CeAu₂Ge₂ vs temperature T . In (a) the data of 3, 1, and 0 T are consecutively upward shifted by 3 J/mol K for clarity. (c) and (d) show the magnetization $M(T)$ of AGF- and SF-CeAu₂Ge₂ samples measured in $B = 0.1$ T (from Ref. 14). The inset of (c) shows $M(T)$ with expanded horizontal and vertical scales to highlight the transition at T_{N2} . Vertical dashed lines indicate the antiferromagnetic transition temperatures T_{N1} and T_{N2} in zero field.

We compare the specific-heat transitions of the two types of samples more closely in Fig. 6. Figure 6(a) shows the low-temperature data of $C_{4f}(T)$ of AGF-CeAu₂Ge₂ in magnetic fields $B = 0, 1, 3,$ and 6 T. For $B = 0$, two anomalies, i.e., a broad maximum and a kink, indicate two transitions as identified by the largest slope in dC_{4f}/dT at $T_{N1} = 12.1$ K and $T_{N2} = 14.5$ K. We attribute them to the antiferromagnetic transitions previously observed in the magnetization $M(T)$ for $B = 0.1$ T parallel to the easy c direction and reproduced in Fig. 6(c).¹⁴ We note that, as indicated by two vertical dashed lines in Figs. 6(a) and 6(c), the high- T transition at 14.5 K coincides with a small change in the slope of $M(T)$, and the low- T transition at 12.1 K coincides with the maximum of M . In an applied magnetic field, T_{N1} and T_{N2} shift to lower temperatures and the specific-heat anomalies broaden and become less pronounced. At 6 T, only a broad hump remains, consistent with the paramagnetic state being fully polarized. The T_{N1} and T_{N2} values are in good agreement with the phase diagram in Fig. 7(a). Toward temperatures below 2.5 K, as shown in Fig. 5, we observe a slight upturn of the specific heat of AGF-CeAu₂Ge₂ which jeopardizes an accurate determination of the Sommerfeld coefficient in the present T range because the intercept of a linear fit in the C/T versus T^2 plot leads to an overestimated value of γ . Low-temperature measurements down to 100 mK are necessary to resolve this issue. The $C_{4f}(T)$ data of SF-CeAu₂Ge₂ in zero field and the corresponding $M(T)$ curves are shown in Figs. 6(b) and 6(d), respectively. In addition to the salient transition at $T_N = 9.2$ K, a weak shoulder around $T = 14$ K, which can also be identified in Fig. 5(b), might indicate that the twofold antiferromagnetic transitions are intrinsic in CeAu₂Ge₂. From the present resistivity and specific-heat data along with our previous magnetization work,¹⁴ we construct a phase diagram

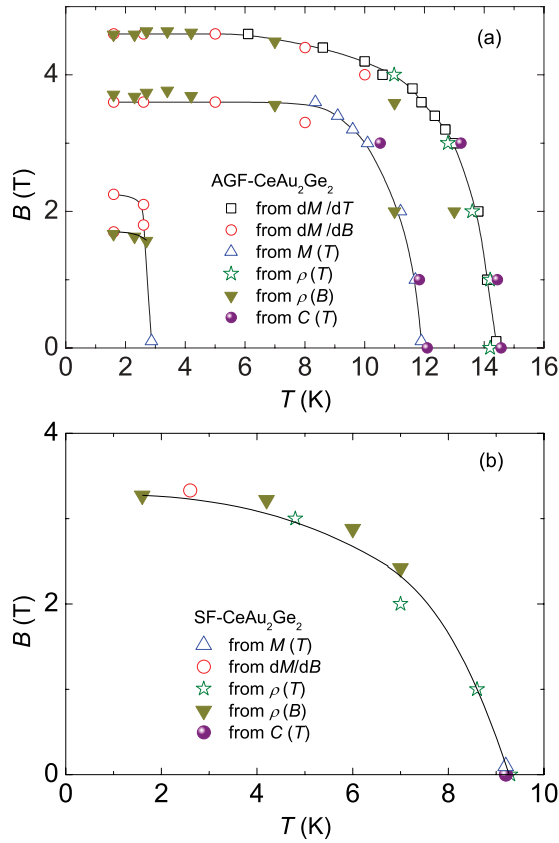


FIG. 7. (Color online) B - T phase diagram of (a) AGF-CeAu₂Ge₂ and (b) SF-CeAu₂Ge₂. The dM/dT , dM/dB , and $M(T)$ data are from Ref. 14.

of SF-CeAu₂Ge₂ in Fig. 7(b), which is comparable to the phase diagram constructed from another batch of the SF sample (VF526 in Ref. 14).

C. Pressure dependence of the magnetization

The magnetization M of AGF-CeAu₂Ge₂ as a function of temperature in an applied field $B = 0.1$ T under different hydrostatic pressures P is shown in Fig. 8(a). At ambient pressure, the maximum of $M(T)$ at $T_{N1} = 12.3$ K signals the antiferromagnetic order, comparable with the previous results on AGF-CeAu₂Ge₂.¹⁴ Due to the appreciable addenda contribution of the CuBe pressure cell, the shoulder indicating the “precursor” transition at T_{N2} (Ref. 14) is hardly visible. Upon applying pressure, the whole feature of $M(T)$ holds, and T_{N1} increases linearly with pressure at a small rate of dT_{N1}/dP of $(4.9 \pm 0.6) \times 10^{-2}$ K/kbar as shown in Fig. 8(b).

Figure 9 shows isothermal $M(B)$ measurements under different pressures up to $B = 8$ T. All data were obtained at $T = 1.6$ K in decreasing fields. For comparison, the data taken at different pressures were normalized to the magnetization value at 8 T. To determine the transition fields, differential plots were used as shown for one example in the inset of Fig. 9. Three steplike transitions at B_{M1} , B_{M2} , and B_C can be observed around 1.85, 3.5, and 4.5 T, respectively, in agreement with the previous results.¹⁴ The transition around $B = 2.2$ T can not be resolved due to the large pressure-cell contribution (see Fig. 8 of Ref. 14). When $0 < B < B_{M1}$, the system stays

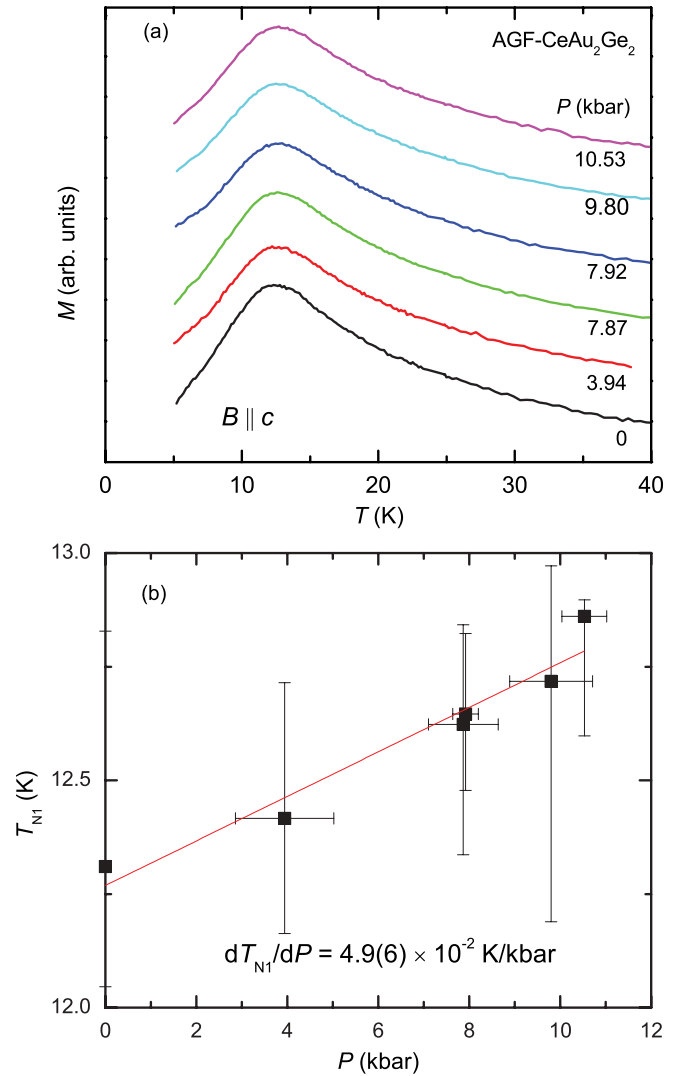


FIG. 8. (Color online) (a) Temperature dependence of the magnetization M from 5 to 40 K at different pressures for AGF-CeAu₂Ge₂ with the magnetic field $B = 0.1$ T parallel to the c axis. (b) Pressure dependence of the antiferromagnetic ordering temperature T_{N1} . Vertical error bars denote the temperature width of 90% of the magnetization maximum. Horizontal bars denote the 10%–90% width of the superconducting transition temperature of Sn serving as a pressure gauge.

at its lowest-energy state, i.e., an Ising-type antiferromagnet. When $B_{M1} < B < B_{M2}$, a fraction of the moments with a direction that is energetically unfavorable flip into the direction favorable with respect to B , resulting in a “ferrimagnetic-like” phase realized as the first rounded plateau with $\approx 1/3$ of the saturation moment M_S . When $B_{M2} < B < B_C$, additional moments flip and form the second rounded plateau close to B_C with $\approx (4/5) M_S$. However, we have to mention that the plateau heights differ from those determined previously.¹⁴ Finally, for $B = B_C$, the magnetization abruptly increases to the value M_S . This jump corresponds to a conventional metamagnetic transition and the transition is first order as has been demonstrated in the magnetic hysteretic behavior.¹⁴

Upon applying pressure, the magnetization value at the plateaux is nearly unaffected, while the transition fields

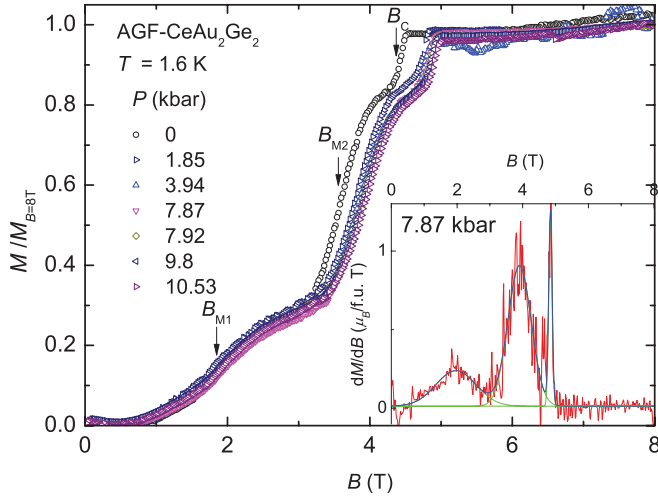


FIG. 9. (Color online) Isothermal field dependence of normalized magnetizations up to 8 T at $T = 1.6$ K under different pressures; the inset shows the dM/dB vs B at 7.87 kbar. Arrows indicate transition fields.

shift slightly. The pressure dependence of the metamagnetic transition fields is shown in Fig. 10. B_{M1} , B_{M2} , and B_C all increase linearly with pressure at a rate of $dB_{M1}/dP = 11 \pm 6$, 13.5 ± 1 , and 19.5 ± 2 mT/kbar, respectively. These fits ignore the steep initial increase of B_{M2} and B_C from ambient pressure to the finite- P data. The origin of the deviation of B_{M2} and B_C at ambient pressure is not clear. After we depressurized the pressure cell, the remnant pressure is 0.02 kbar, and the values of B_{M2} and B_C (open symbols in Fig. 10) are 0.2 T larger than those measured when we initially clamped the pressure cell, i.e., $P = 1$ bar (solid symbols). However, B_{M2} and B_C retain the same values when we finally measured the sample which is removed from the pressure cell (half-filled symbols). This result is quantitatively in line with the fact that the isothermal magnetization curves from two batches of the AGF sample (VF 474 and 527 in Fig. 3 of Ref. 14) show different B_{M2} and B_C but the same B_{M1} . This indicates that slight differences in structural factors, e.g., lattice constant, bonding angle, dislocation, etc., could affect B_{M2} and B_C more strongly than B_{M1} .

To discuss the volume dependence of the characteristic energy scale, the bulk modulus $B \equiv -V \times (dP/dV)$ needs to be known. Since there is no available experimental data of CeAu_2Ge_2 at present, we adopt the value $B = 1313$ kbar at 10 K from the sister compound CeCu_2Ge_2 .²⁰ The resulting Grüneisen parameter of T_N , $\Gamma_{N1} \equiv -d \ln T_{N1}/d \ln V$ turns out to be 5.2. The Grüneisen parameters of the transition fields B_M , $\Gamma_M \equiv -d \ln B_M/d \ln V$ are estimated to 7.8, 4.6, and 4.9 for B_{M1} , B_{M2} , and B_C , respectively, using the linear fits shown in Fig. 9. The fact that the values of Γ_{N1} and Γ_B agree within $\sim 50\%$ suggests that T_N and B_M represent the same energy scale that depends on the sample's volume. Hence, the antiferromagnetic correlations provide the primary energy scales, while the Kondo energy scale appears to be of less importance.

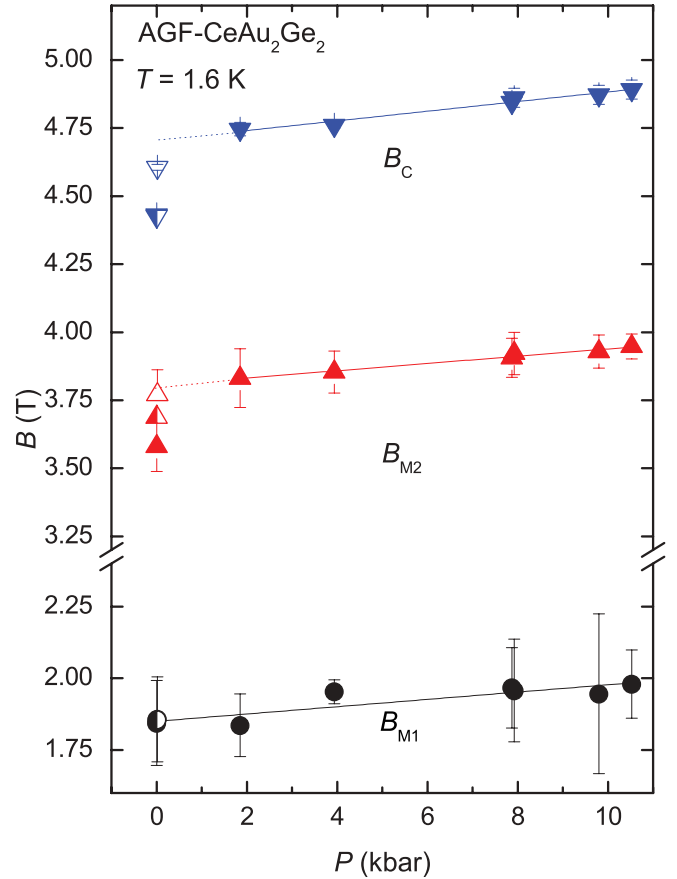


FIG. 10. (Color online) Pressure dependence of the metamagnetic transition fields B_{M1} (circles), B_{M2} (triangles), and the critical field B_C (inverted triangles) in $\text{AGF-CeAu}_2\text{Ge}_2$. Around ambient pressure, solid symbols are the data taken when the sample is just mounted in the pressure cell; open symbols are the data taken after the sample is depressurized; half-filled symbols are the data taken when the sample is removed from the pressure cell.

IV. DISCUSSION

In Ce compounds, the competition of Kondo compensation of local moments and magnetic RKKY coupling between these moments is of primary importance. Although the existence of a Kondo energy scale in CeAu_2Ge_2 was inferred from neutron-diffraction measurements ($T_K < 1$ K),¹² experimental evidence from thermodynamic or transport measurements is lacking. The Kondo energy scale is negligible and hence the RKKY interaction is dominant, implying that J , the exchange energy between conduction electrons and local moments, is small. The application of pressure increases the hybridization and pushes T_N in the Doniach diagram from small J to larger J [$T_N = J^2 N(E_F)$, where $N(E_F)$ is the unnormalized conduction-band density of states at the Fermi energy E_F], while the Kondo effect still is exponentially weak. Similar results of a stabilization of magnetic order with pressure have also been observed in other isostructural compounds such as CeRu_2Ge_2 and CeRh_2Ge_2 , with $dT_N/dP = 0.13$ and 0.16 K/kbar, respectively.²¹ The positive dT_N/dP of CeAu_2Ge_2 is in line with the observation that by replacing Au with Ag, the unit-cell volume is enlarged by $\approx 1\%$ and T_N is lowered to 6.3 K.¹²

To describe the spin configurations of antiferromagnetic systems with several phase transitions induced by magnetic field, the $2n$ -sublattice model with n an integer is often used to account for fractional magnetizations in the intermediate states. For example, $1/2$ and $1/3$ of the saturation magnetization M_S in $M(B)$, i.e., “ $\uparrow\downarrow\uparrow\uparrow$ ” for $n = 2$ and “ $\uparrow\downarrow\uparrow\downarrow\uparrow\uparrow$ ” for $n = 3$ where \uparrow and \downarrow correspond to spin-up and spin-down sublattices, respectively, were observed in four- and six-sublattice systems.^{22,23} The plateaux of CeAu₂Ge₂ in this study are not well defined and can not be explained by simple n -sublattice models. A recent elastic neutron-scattering study revealed incommensurate magnetic reflections in the temperature range $2.5 < T < 8.5$ K in addition to the commensurate antiferromagnetism.²⁴ This is roughly the same T range where we observed several transitions in the isothermal magnetization $M(B)$ from which we constructed the phase diagram of Fig. 7. Indeed, the neutron-scattering data suggest the existence of at least one such transition in this T range.²⁴ The competition between commensurate and incommensurate phases under magnetic field might well be affected by disorder, which could explain the topological differences of the phase diagrams of AGF and SF samples, as well as the different plateau heights of samples within the AGF family. Thus, to clarify the exact physics behind these differences, experiments on high-quality single crystals with fewer inclusions, which might affect the stability of metamagnetic phases, are necessary. Microscopic measurements, in particular detailed neutron-scattering studies of the field-induced magnetic phases, are expected to give a final clue to the complete determination of the intrinsic spin structures in CeAu₂Ge₂.

Aside from the different types of phase diagrams, there are notable differences in the critical temperatures and critical fields: $T_{N1} = 12.1$ K, $T_{N2} = 14.5$ K (AGF), $T_N = 9.2$ K (SF), with a small shoulder at 14 K observed in the specific heat; $B_C(T \rightarrow 0) = 4.6$ T (AGF), $B_C(T \rightarrow 0) = 3.3$ T (SF). These differences by $\sim 30\%$ call for special attention. The differences in the structure lead to an overall decrease of the unit-cell volume by 0.77% when going from AGF to SF samples (see Ref. 14). BF samples show nearly the same V reduction ($\sim 0.6\%$) but have similar T_N and B_C values as AGF samples. From our pressure data on the AGF sample one would infer that T_N and B_C would be larger for SF than for AGF samples. However, the opposite behavior is observed. This points to the decisive role of the Ce-Au hybridization affecting J . Since we are on the low- J side of the Doniach diagram as indicated by $dT_N/dP > 0$, any weakening of the hybridization would lead to a decrease of J . We have previously determined that

the Au site has an 8% deficit of occupation. It is well known that in CeT₂X₂ systems the $4f$ -electron–conduction-electron hybridization is determined to a large extent by the Ce nearest neighbor T . This deficiency in hybridization might well be the origin of the different behavior of AGF and SF samples, while at the same time it is not expected to change the crystalline anisotropy to a large extent. In addition, in the SF sample, an impurity effect has been shown to dominate the present magnetoresistance data, and Sn impurities might also affect the Ce-Au hybridization. This underlines the necessity of a new generation of crystals to resolve this issue.

V. CONCLUSION

The work presented here complements our previous work on the magnetic properties of CeAu₂Ge₂ and highlights the important effect of the flux used to prepare single crystals. The resistivity of the tin-flux grown (SF) sample shows strong impurity effect from inclusions. For the Au-Ge flux-grown (AGF) samples, the specific heat clearly shows two antiferromagnetic transitions at $T = 12.1$ and 14.5 K, which are in accord with the phase diagram obtained from previous magnetization measurements and confirm the complex spin states of AGF-CeAu₂Ge₂. The SF sample shows only a single sharp transition at $T = 9.2$ K in the specific heat, and only a very weak feature at 14 K.

The antiferromagnetic ordering temperature T_N of AGF-CeAu₂Ge₂ increases linearly under hydrostatic pressure. The pressure monotonically reduces the unit-cell volume and hence enhances the RKKY interaction, while the Kondo effect is still very weak. In the isothermal magnetization, three field-induced transitions are observed, and the transition fields increase upon applying pressure. By adopting the value of bulk modulus of the isostructural compound CeCu₂Ge₂, Grüneisen parameters of T_N and B_M are calculated and have the same magnitude, indicating that antiferromagnetic correlations set the energy scale of transition temperature and critical field. In order to shed more light on the differences, detailed neutron-scattering studies on well-characterized samples are necessary. Thermal expansion measurements will be performed that will yield information about the strain dependence of T_N and the critical field.

ACKNOWLEDGMENTS

We thank B. Pilawa and K. Grube for helpful discussions. This work was supported by the Deutsche Forschungsgemeinschaft through the Research Unit FOR 960.

*chien-lung.huang@kit.edu

¹A. S. Sefat, A. M. Palasyuk, S. L. Bud'ko, J. D. Corbett, and P. C. Canfield, *J. Solid State Chem.* **181**, 282 (2008).

²P. Gegenwart, F. Kromer, M. Lang, G. Sparn, C. Geibel, and F. Steglich, *Phys. Rev. Lett.* **82**, 1293 (1999).

³F. Steglich, J. Aarts, C. D. Bredl, W. Lieke, D. Meschede, W. Franz, and H. Schäfer, *Phys. Rev. Lett.* **43**, 1892 (1979).

⁴D. Jaccard, K. Behnia, and J. Sierro, *Phys. Lett. A* **163**, 475 (1992).

⁵N. D. Mathur, F. M. Grosche, S. R. Julian, I. R. Walker, D. M. Freye, R. K. W. Haselwimmer, and G. G. Lonzarich, *Nature (London)* **394**, 39 (1998).

⁶P. Haen, J. Flouquet, F. Labpierre, P. Lejay, and G. Rememyi, *J. Low Temp. Phys.* **67**, 391 (1987).

⁷S. Doniach, *Phys. B (Amsterdam)* **91**, 231 (1977).

⁸D. Jaccard, P. Link, E. Vargoz, and K. Alami-Yadri, *Phys. B (Amsterdam)* **230-232**, 297 (1997).

- ⁹A. Severing, E. Holland-Moritz, and B. Frick, *Phys. Rev. B* **39**, 4164 (1989).
- ¹⁰O. Stockert, E. Faulhaber, G. Zwicknagi, N. Stüßer, H. S. Jeevan, M. Deppe, R. Borth, R. Küchler, M. Loewenhaupt, C. Geibel *et al.*, *Phys. Rev. Lett.* **92**, 136401 (2004).
- ¹¹E. Lengyel, M. Nicklas, H. S. Jeevan, C. Geibel, and F. Steglich, *Phys. Rev. Lett.* **107**, 057001 (2011).
- ¹²A. Loidl, K. Knorr, G. Knopp, A. Krimmel, R. Caspary, A. Böhm, G. Sparn, C. Geibel, F. Steglich, and A. P. Murani, *Phys. Rev. B* **46**, 9341 (1992).
- ¹³D. A. Joshi, A. K. Nigam, S. K. Dahr, and A. Thamizhavel, *J. Magn. Mater.* **322**, 3363 (2010).
- ¹⁴V. Fritsch, P. Pfundstein, P. Schweiss, E. Kampert, B. Pilawa, and H. v. Löhneysen, *Phys. Rev. B* **84**, 104446 (2011).
- ¹⁵U. Rauchschalbe, F. Steglich, and H. Rietschel, *Phys. B (Amsterdam)* **148**, 33 (1987).
- ¹⁶H. Miyagawa, G. Oomi, M. Ohashi, I. Satoh, T. Komatsubara, M. Hedo, and Y. Uwatoko, *Phys. Rev. B* **78**, 064403 (2008).
- ¹⁷A. P. Pikul, D. Kaczorowski, T. Plackowski, A. Czopnik, H. Michor, E. Bauer, G. Hilscher, P. Rogl, and Y. Grin, *Phys. Rev. B* **67**, 224417 (2003).
- ¹⁸F. Heringhaus and T. A. Painter, *Mater. Lett.* **57**, 787 (2002).
- ¹⁹K. Kadowaki and S. B. Woods, *Solid State Commun.* **58**, 507 (1986).
- ²⁰A. Onodera, S. Tsuduki, Y. Ohishi, T. Watanuki, K. Ishida, Y. Kitaoka, and Y. Onuki, *Solid State Commun.* **123**, 113 (2002).
- ²¹J. D. Thompson, Y. Uwatoko, T. Graf, M. F. Hundley, D. Mandrus, C. Gordart, L. C. Gupta, P. C. Canfield, and A. Migliori, *Phys. B (Amsterdam)* **199-200**, 589 (1994).
- ²²L. Holmes, R. Sherwood, and L. G. V. Uitert, *J. Appl. Phys.* **39**, 1373 (1968).
- ²³A. Narath, *Phys. Rev.* **139**, 1221 (1965).
- ²⁴D. K. Singh, A. Thamizhavel, J. W. Lynn, S. K. Dhar, and T. Hermann, *Phys. Rev. B* **86**, 060405(R) (2012).